Pillars and globules at the edges of H II regions: confronting *Herschel* observations and numerical simulations

Journal Item

Version: Proof

Link(s) to article on publisher's website:
http://dx.doi.org/doi:10.1051/0004-6361/201322233
http://www.aanda.org/articles/aa/abs/2013/12/aa22233-13/aa22233-13.html

Astronomy & Astrophysics manuscript no. main
November 18, 2013

Pillars and globules at the edges of H II regions

Confronting *Herschel*⋆ observations and numerical simulations

P. Tremblin[1,2], V. Minier[1], N. Schneider[3,4], E. Audit[1,5], T. Hill[1], P. Didelon[1], N. Peretto[6], D. Arzoumanian[7], F. Motte[1], A. Zavagno[8], S. Bontemps[3,4], L. D. Anderson[9], Ph. André[1], J. P. Bernard[10], T. Csengeri[11], J. Di Francesco[12], D. Elia[13], M. Hennemann[1], V. Könyves[1,7], A. P. Marston[14], Q. Nguyen Luong[15], A. Rivera-Ingraham[16,17], H. Roussel[18], T. Sousbie[18], L. Spinoglio[19], G. J. White[20,21], and J. Williams[22]

(Affiliations can be found after the references)

November 18, 2013

ABSTRACT

Context. *Herschel* far-infrared imaging observations have revealed the density structure of the interface between H II regions and molecular clouds in great detail. In particular, pillars and globules are present in many high-mass star-forming regions, such as the Eagle nebula (M16) and the Rosette molecular cloud, and understanding their origin will help characterize triggered star formation.

Aims. The formation mechanisms of these structures are still being debated. The initial morphology of the molecular cloud and its turbulent state are key parameters since they generate deformations and curvatures of the shell during the expansion of the H II region. Recent numerical simulations have shown how pillars can arise from the collapse of the shell in on itself and how globules can be formed from the interplay of the turbulent molecular cloud and the ionization from massive stars. The goal here is to test this scenario through recent observations of two massive star-forming regions, M16 and the Rosette molecular cloud.

Methods. First, the column density structure of the interface between molecular clouds and associated H II regions was characterized using column density maps obtained from far-infrared imaging of the *Herschel* HOBYS key programme. Then, the DisPerSe algorithm was used on these maps to detect the compressed layers around the ionized gas and pillars in different evolutionary states. Column density profiles were constructed. Finally, their velocity structure was investigated using CO data, and all observational signatures were tested against some distinct diagnostics established from simulations.

Results. The column density profiles have revealed the importance of compression at the edge of the ionized gas. The velocity properties of the structures, i.e. pillars and globules, are very close to what we predict from the numerical simulations. We have identified a good candidate of a nascent pillar in the Rosette molecular cloud that presents the velocity pattern of the shell collapsing on itself, induced by a high local curvature. Globules have a bulk velocity dispersion that indicates the importance of the initial turbulence in their formation, as proposed from numerical simulations. Altogether, this study re-enforces the picture of pillar formation by shell collapse and globule formation by the ionization of highly turbulent clouds.

Key words. ISM: individual objects (M16, Rosette) - Stars: formation - H II regions - ISM: structure - ISM: kinematics and dynamics - Methods: observation

1. Introduction

H II regions can have very complex shapes depending on the distribution of the ionizing sources and the initial structures in the surrounding gas. They range from spherical bubbles (e.g. Deharveng et al. 2009, for RCW120), bipolar nebulae (e.g. RCW 36 Minier et al. 2013) to complex and large regions like Cygnus X OB2 and OB9 (see Schneider et al. 2012b). Dense layers of gas and dust are observed at the interface between the H II regions and their parent molecular cloud, and they consist of various structures. Condensations of cold gas are often present in these layers (e.g. Deharveng et al. 2010). Furthermore, Thompson et al. (2012) shows that massive young stellar objects (YSOs) are often observed on the edge of the bubbles and that 15-30 % of massive stars could be formed in those regions. Elongated columns (pillars) of gas are observed pointing towards the ionizing sources and are usually connected to the molecular cloud (e.g. Hester et al. 1996, for "the Pillars of Creation"). Unlike pillars and condensations, cometary globules are bubbles of cold gas that are inside the H II region and disconnected from the molecular cloud (e.g. White & Gee 1986; White 1993; Thompson et al. 2004; Schneider et al. 2012b). Understanding the origin of these different structures is very important for characterizing triggered star formation and the impact of massive stars on the initial mass function (IMF).

Various scenarios have been investigated to explain the formation mechanism of these structures. The collect and collapse scenario (see Elmegreen & Lada 1977) proposes that the shell becomes sufficiently dense thanks to cooling of the swept-up gas, to reach the gravitational instability and therefore form dense condensations. This scenario leads to a sequential star formation observed in many regions (e.g. Blaauw 1991). Bertoldi (1989) proposed that cometary globules could be the result of the radiative implosion of an isolated gravitationally stable clump. More recently, this scenario has been tested further using numerical simulations (Miao et al. 2006, 2009, 2010; Bisbas et al. 2011; Haworth & Harries 2011). Mackey & Lim (2010) shows that the shadowing effect of such clumps in the density field

⋆ *Herschel* is an ESA space observatory with science instruments provided by European-led Principal Investigator consortia and with important participation from NASA.

Correspondence to: pascal.tremblin@cea.fr

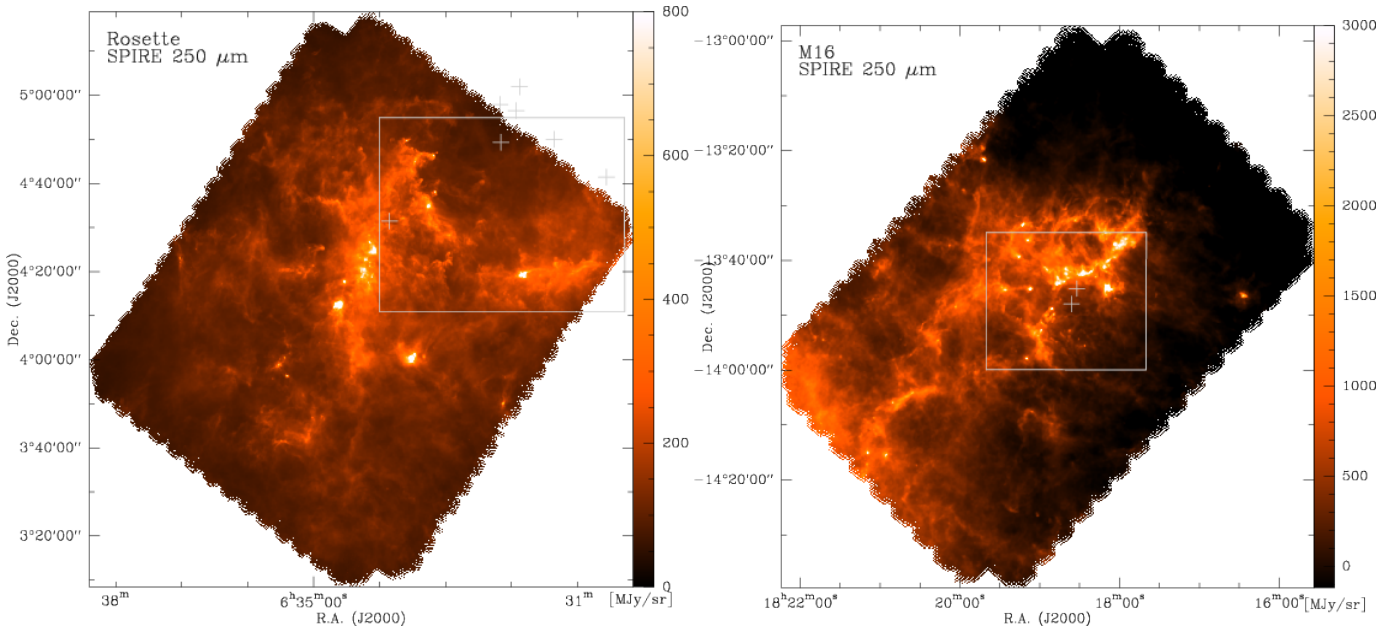

Fig. 1. *Herschel* SPIRE 250 μm image of the Rosette (left) and M16 (right) molecular cloud with the studied areas outlined in grey (see Figs. 2 and 4 for Rosette and Figs. 7 and 9 for M16). The position of the main ionizing sources (O stars) are indicated with the grey crosses. The flux scale is in [MJy/sr].

could also form pillars. All these studies have shown how the gravitational collapse of a stable cloud can lead to triggered star formation. However, using cloud-scale simulations, Dale et al. (2013) shows that it can be problematic to distinguish triggered from pre-existing star formation. Also recently, parsec-scale simulations have shown that most of the observed structures can be formed from the interaction between the turbulence of the molecular cloud and the ionization (Mellema et al. 2006; Arthur et al. 2011; Gritschneder et al. 2010; Walch et al. 2013). However it is often difficult to understand the precise mechanisms at the origin of the different structures in these complex simulations.

Tremblin et al. (2012a) proposed that the important parameter for forming pillars and clumps at the interface is the degree of curvature of the dense shell perturbed by pre-existing structures. A high curvature triggers the collapse of the shell into itself to form pillars, whereas low curvature only triggers the formation of dense clumps that are accelerated with the shell and remain in the shell. This scenario has since been tested for turbulent media (see Tremblin et al. 2012b) in which the level of turbulence (compared to the pressure of the H II region) has been identified as a key ingredient in the formation of cometary globules. These simulations do not take the FUV photons and the subsequent PDRs and temperature gradients in the cold gas into account. Many observational diagnostics based on the density and velocity structures of the compressed cold gas at the interface have been derived to test these models:

- Shell fragments are compressed layers of gas formed by the expansion of the ionized gas, and they can be identified by an excess in the column-density maps.
- A nascent pillar can be identified thanks to a red-shifted and blue-shifted component in the velocity spectrum of the parts of the shell that are locally collapsing. The velocity shift between the two peaks should be twice the velocity of the globally expanding shell. An evolved pillar shows a single peak at the velocity of expansion of the shell.
- A globule formed from the interaction of the turbulence and the ionization has a line-of-sight velocity shifted at high velocities compared to those of nearby dense shell fragments and pillars.

The present paper aims at scrutinizing these diagnostics using *Herschel* observations of the Rosette Nebula and the Eagle nebula (M16) taken as part of the HOBYS key project[1] (Herschel imaging survey of OB Young Stellar objects, Motte et al. 2010). These two regions (overview in Fig. 1) present a complex interface with pillars, globules, and compressed layers. They have a similar total ionizing flux and therefore are perfect laboratories for testing the diagnostics derived from the simulations. We first investigate in Sects. 2 and 3 the density structure of the interface between the molecular and ionized gas by tracing the crests of the densest parts (named dense fronts hereafter) of column density maps using the DisPerSe algorithm (Sousbie 2011), and study their profiles. Using molecular gas tracers, we then study the bulk velocity of the pillars, clumps, and globules that are present in these regions. Finally (Sect. 4), we compare these observations with the curvature model proposed in Tremblin et al. (2012a) for the formation of pillars and dense clumps, and the turbulent one proposed in Tremblin et al. (2012b) for the formation of globules.

2. The Rosette nebula

The Rosette molecular cloud is located at 1.6 kpc from the Sun (Williams et al. 1994; Schneider et al. 1998a; Heyer et al. 2006). The central cluster NGC 2244 is dominated by 17 OB stars that have a total Lyman-α luminosity of $3.8{\times}10^5$ $L_\odot$ (see Cox et al. 1990). Photon-dominated regions (PDRs) are detected deep inside the cloud (see Schneider et al. 1998b). The infrared (IR) population of the molecular cloud was investigated in near- and

[1] The *Herschel* imaging survey of OB Young Stellar objects (HOBYS) is a *Herschel* key program. See `http://hobys-herschel.cea.fr`

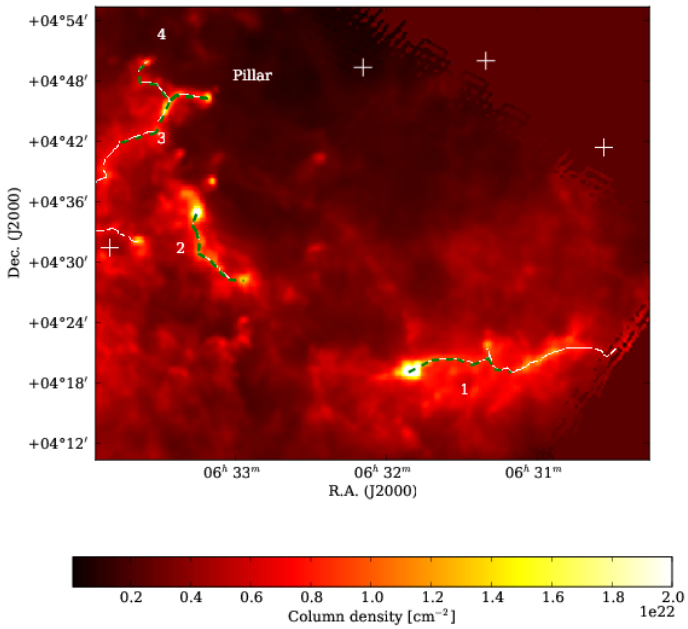

Fig. 2. Column density map (with 37″ resolution) of the interface between the Rosette molecular cloud and the H II region around NGC 2244. The DisPerSe skeleton is drawn in white, and each part of the dense layer is labelled from 1 to 4. The pillar is identified as a segment with one side connected by a triple point to the dense fronts 3 and 4, and the opposite side is disconnected and points toward the ionizing sources. The parts of the skeleton used for the profiles in Fig. 3 are indicated with the green dashed lines. The position of the main ionizing sources (O stars) are indicated with the white crosses.

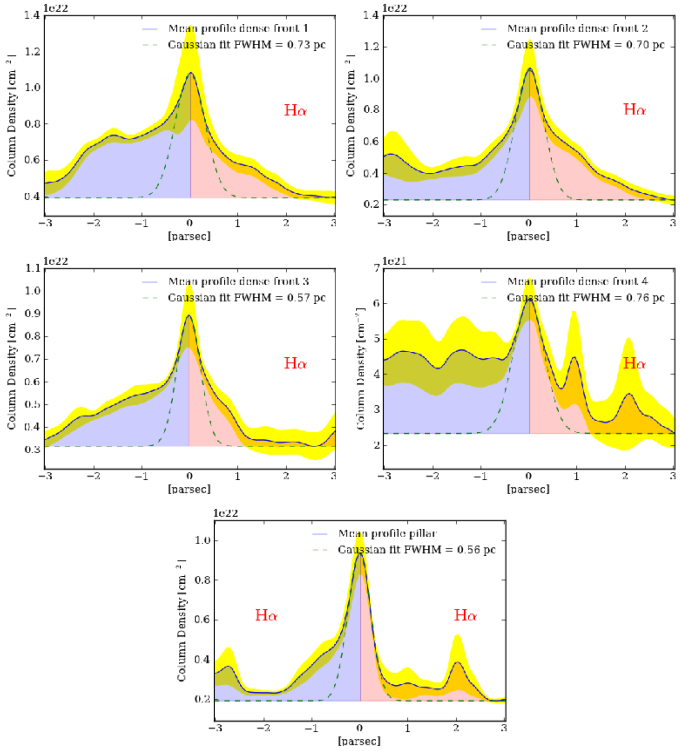

Fig. 3. Profiles of the dense fronts and pillars traced by DisPerSe in the Rosette Molecular cloud. The extension of the profiles is fixed at 3 parsecs. The yellow shaded area represents the standard deviation of the profiles. The red sign Hα indicates on which side ionized gas is present (see also Fig. 4 and the Hα emission). The green-dashed curve is the Gaussian fit used to determine the FWHM width.

dense front	FWHM (pc)	$\sigma_{FWHM}(pc)$	Asymmetry	σ_{asym}
1	0.75	0.29	1.8	0.4
2	0.69	0.20	1.4	0.6
3	0.57	0.27	1.6	0.8
4	0.76	0.23	2.2	1.4
pillar	0.55	0.05	1.8	1.0

Table 1. Deconvolved FWHM width and asymmetric parameter for the averaged profiles of the 5 dense fronts in the Rosette Molecular cloud. The asymmetric parameter is the ratio of the blue area to the red area in the profiles in Fig. 3.

mid-IR surveys (see Poulton et al. 2008, and references therein). More recently, the Rosette molecular cloud was studied using far-IR *Herschel* observations (see Schneider et al. 2010, 2012a; Hennemann et al. 2010; Motte et al. 2010; Di Francesco et al. 2010). Figure 1 provides as an overview an improved SPIRE 250 μm map of the Rosette cloud, reduced with the pipeline in HIPE10[2], which includes a destriping module with baseline subtraction, correction for extended emission, and an absolute flux calibration using the ZEROPOINTCORRECTION task in HIPE10 to obtain the offset values from Planck. The PACS 70 and 160 maps were produced using the HIPE pipeline and the Scanamorphos sotware package (Roussel 2012).

In Sect. 2.1 we investigate the H_2 column density structure of the edge of the molecular cloud using the *Herschel* map with an angular resolution of 37″ (0.26 pc). We checked the width of the pillar in the north-east of the map using the 70 μm data (resolution of $\sim$ 6″). The 70 μm can be used as a tracer of the warm dust in the photo-dissociation region (PDR) and therefore as an indicator of the width of the cold structures surrounded by the PDR. The resulting width is similar, and the structures are therefore well resolved at the edge of the cavity. In Sect. 2.2 we concentrate on the velocity structure of three subregions of the interface: the pillar (east of the cavity), the globules (also east), and the southern part of the dense front.

[2] http://herschel.esac.esa.int/hipe

2.1. Column density structure

The column density map of the Rosette cloud was made by fitting pixel-by-pixel the spectral energy distribution (SED) of a greybody to the *Herschel* wavebands between 160 and 500 μm (at the same 37″ resolution), assuming the dust opacity law of Hildebrand (1983) and an emissivity spectral index of $\beta = 2$. The 70 μm data are not used to derive the column density since it does not entirely trace the cold dust. See Schneider et al. (2012a) for more details. The resulting column density map obtained from *Herschel* data covers a wider density range and is thus more representative than column density maps obtained from molecular line data because there is no cut-off at high or low densities as is the case for, say, ^{13}CO (see Carlhoff et al. 2013, for a detailed comparison in W43). Figure 2 shows the column density map of the interface between the Rosette molecular cloud and the H II region around NGC 2244. We then applied the DisPerSe algorithm

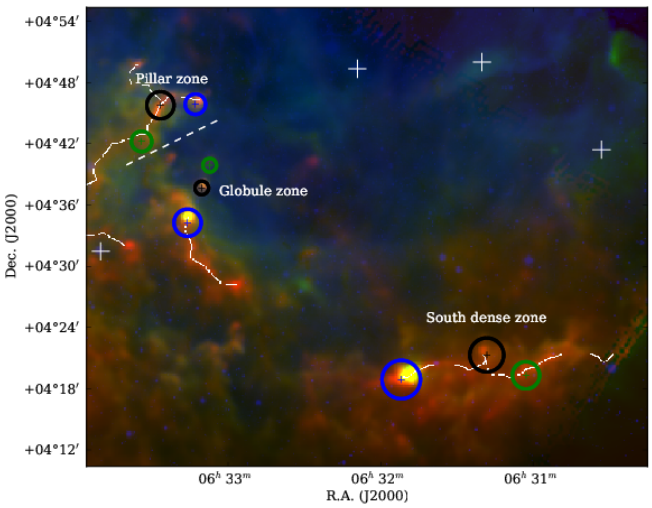

Fig. 4. Three-color image of the interface between the Rosette molecular cloud and the H II region around NGC 2244 (red: *Herschel* column density map, green: PACS 70 μm, blue: Hα). The white crosses indicate the O stars. Each spectrum in Fig. 5 is integrated inside the corresponding colored circles. The centre and radius of each circle are chosen by taking the peak value and the extension of the CO emission. The white dashed line is an indication for the separation between the pillar and globule zones.

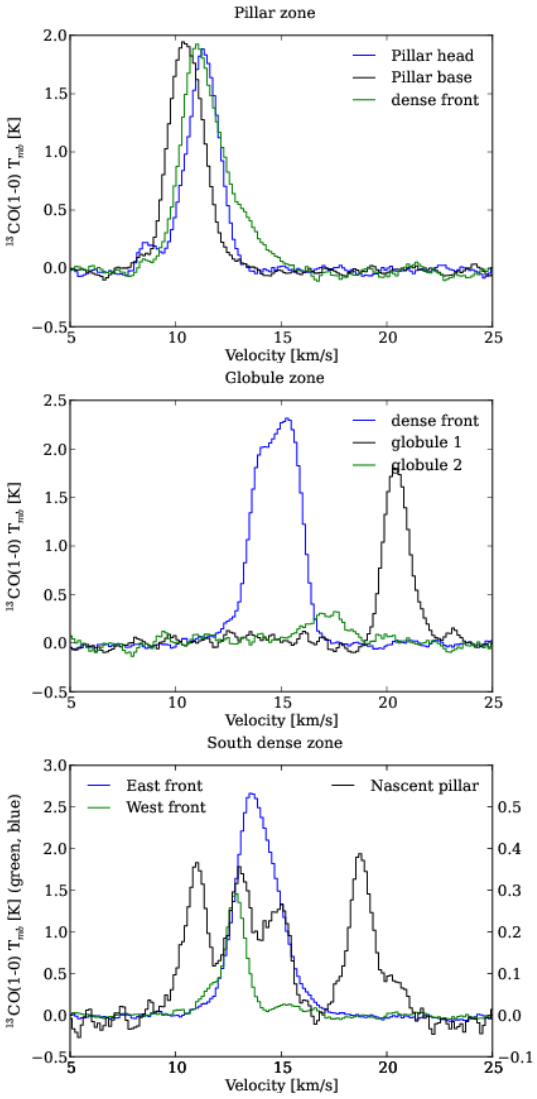

Fig. 5. ^{13}CO (1-0) integrated spectra in the three sub-regions of the interface in the Rosette molecular cloud. The spectra are spatially integrated in the colored circles showed in Fig. 4. The temperature scale for the nascent pillar area on the South dense zone is multiplied by a factor of five.

(Sousbie 2011): a general method, based on principles of computational topology that traces filaments by connecting saddle points to maxima with integral lines. DisPerSe was used with an intensity contrast level of 4×10^{21} cm^{-2} and a low-density threshold of 5×10^{21} cm^{-2}. These parameters were chosen to trace only the crests of the main parts of the dense front that can be identified by eye on the column density map. As outlined in Schneider et al. (2012a), a lower density contrast (e.g. $\sim0.5\times10^{21}$ cm^{-2}) results in a very filamentary structure, while higher values lead to identifying of only the main features.

The dense fronts are labelled from 1 to 4 in Fig. 2. A recent survey of far-IR clumps in the Rosette cloud (White et al. in prep.) shows that the bright far-IR source at the left-hand edge of dense front 1 shows H_2O maser emission, an observational signature that indicates star formation. The pillar and the dense fronts 3 and 4 are connected, forming a triple point (the connection between three lines) in the skeleton. Another triple point is seen in the middle of the dense front 1. We performed transverse column density profiles along a piecewise linear segmentation of the DisPerSe skeleton following a similar procedure to the one, say, in Arzoumanian et al. (2011). Figure 3 presents the averaged profiles on the dense fronts and on the pillar.

We fitted the inner part of the dense fronts with Gaussian functions after subtracting a background set at the minimum of the fitted profile. The level of the background does affect the width of the Gaussian profile, however other choices of the background level only induce small variations in the width as also found in Peretto et al. (2012). The definition used here leads to a background around the same level in all of the profiles considered $N_{H_2} \approx 2-4\times10^{21}$ cm^{-2}. This approach is also similar to the work of Arzoumanian et al. (2011) and Hennemann et al. (2012). There are two possibilities for determing the full width at half maximum (FWHM): fitting Gaussian profiles at each position along the front and taking the mean value or fitting a Gaussian profile on the averaged profiles in Fig. 3. We used both strategies, and the FWHM values along the fronts are given in Table 1 (deconvolved with the beam of the telescope). The average and standard deviation of the width along the fronts is weighted by the inverse of the standard deviation of the fit at each position along the front.

The computed widths are in good agreement with the widths of the average profiles given in Fig. 3. For example, the averaged values of the deconvolved FWHM are 0.75 ± 0.3 pc for the dense front 1 and 0.55 ± 0.05 pc for the pillar. These values are 3 % different from the width of the averaged profile in Fig. 3 so they fit within the error bars. The widths of the pillar and the dense front 3 are smaller than values for other parts of the front. Since these two structures are parallel to the direction of the expansion of the H II region, and the other dense fronts are perpendicular, a possible explanation is that the perpendicular dense fronts accumulate more gas during the expansion, while this is not possible for elongated structures parallel to the direction of expansion.

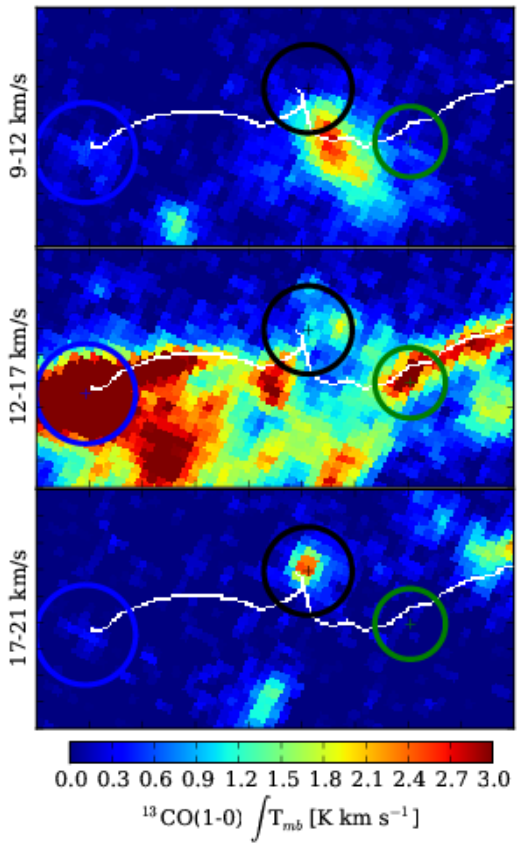

Fig. 6. ^{13}CO (1-0) integrated channel maps of the south dense zone around the three main velocity components: 9-12 km/s, 12-17 km/s, and 17-21 km/s.

Similar to Peretto et al. (2012), we defined an asymmetric parameter as the ratio of the integrated column density on either side of the profile peak (background subtracted). It corresponds to the blue area over the red area in Fig. 3, and the values for the different profiles are indicated in Table 1. The dispersion is the standard deviation of the parameter value along the fronts. The dense fronts are systematically asymmetric with less gas on the side that is exposed to ionized gas (indicated by the red Hα in Fig. 3). The profile of the pillar is also asymmetric, however we see in Sect. 3 that there is no preferential side for the asymmetry in a pillar profile.

2.2. Velocity structure

The bulk velocity of the objects in the interface was investigated using a ^{13}CO (1-0) map obtained with the FCRAO[3] (see Heyer et al. 2006), with an angular resolution of 45″ at 115 GHz. We concentrated our study on the bulk velocity of the main components of the spectra that will be used to compare with models in Sect. 4. The three different regions considered are named pillar, globule, and southern dense zones hereafter, and they are indicated in Fig. 4. The areas in which integrated spectra are indicated in the three-color image in Fig. 4 and the corresponding spectra are presented in Fig. 5.

In the **pillar zone**, the blue spectrum is integrated around the head of the pillar, the black one around the triple point connecting the pillar to the dense fronts 4 and 5, and the green one is integrated on a part of the dense front 5. The main components of the spectra are centred on the same velocity of 10-11 km s^{-1}. Dense front 4 is also connected to the pillar and has a similar velocity. Therefore, the pillar and the connected fronts have a velocity similar to the expansion velocity of the bubble.

The blue spectrum in the **globule zone** is integrated around a clump in the dense front 2, and the black and green ones are integrated around the globules 1 and 2 north of the front. Dense front 2 is a nearby dense region associated with the molecular cloud. In Schneider et al. (1998a), a high angular resolution Hα image was shown with an overlay of ^{13}CO (2-1) emission (their Fig. 15). It clearly shows that the two globules are illuminated by the OB cluster, similar to what is seen at the edge of the dense front. Thus, despite the higher velocity of the globule 1 (∼21 km s^{-1}) with respect to the bulk emission of the dense front of 15 km s^{-1}, the globule is close to the dense front. The globules have velocities red-shifted by +3 and +6 km s^{-1} relative to the nearby front, whereas the pillar has the same velocity as the connected fronts. Therefore the pillar follows the expansion of the bubble, while the globules have motions that are not related to the direction of expansion.

In the **south dense zone**, the blue and green spectra indicate the mean velocity of the western and eastern parts of the dense front, respectively. The western part has a velocity in the range 14-15 km s^{-1}, the eastern part of the order of 13 km s^{-1}. These two velocity components join at the triple point, which was previously identified in the DisPerSe skeleton (see Fig. 2) where the black spectrum is integrated (see Fig. 4). Moreover, there are two other velocity components in the black spectrum, i.e. at 11 km s^{-1} and 19 km s^{-1}. This complex velocity structure with several components also becomes obvious in channel maps over the three main velocity ranges shown in Fig. 6. The bulk emission of the cloud at ∼12-17 km s^{-1} mainly corresponds to the column density map obtained from *Herschel*, and the DisPerSe filament tracing identifies this component. South of the triple point marked black, however, we identify a gas reservoir at lower velocities, and at the northern ending tip of the DisPerSe skeleton there is a smaller region at higher velocities. This characteristic velocity distribution fits into theoretical predictions for pillar formation and is discussed in more detail in Sect. 4.

3. Eagle nebula

The Eagle nebula (M16) is located in the constellation of Serpens at 1.8 kpc from the Sun (Bonatto et al. 2006). A young stellar cluster NGC 6611 is ionizing the molecular gas of this star-forming region. The principal ionizing sources are O4 and O5 stars whose combined ionizing flux is of the order of 2×10^{50} s^{-1} (Hester et al. 1996; White et al. 1999). The discovery of pillars of gas by the *Hubble* space telescope (Hester et al. 1996) popularized this region with the name of "Pillars of Creation". The region is chemically rich, and spectral line studies of the region are numerous (see Pound 1998; White et al. 1999; Allen et al. 1999; Urquhart et al. 2003; Schuller et al. 2006; Linsky et al. 2007, among others). Recently, Flagey et al. (2011) have studied the dust SED using *Spitzer* data. They show that the SED cannot be accounted for by interstellar dust heating by UV radiation, but an additional source of heating is needed to match the mid IR flux. They propose two possible origins: stellar winds or a supernova remnant. *Herschel* provides new observations of the region, and Hill et al. (2012) studied the impact of the ionizing source in detail on the initial temperature of pre-stellar cores lo-

[3] Five College Radio Astronomy Observatory

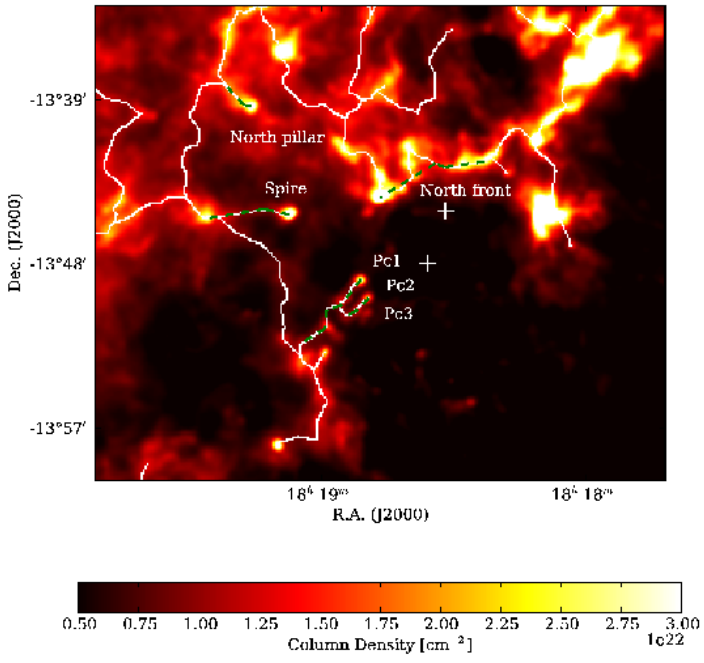

Fig. 7. Column density map of the interface between the Eagle Nebula and the H II region around NGC 6611 (resolution of 25″). The DisPerSe skeleton is drawn in white. The intensity contrast level is 4×10^{21} cm^{-2} and the low-density threshold is 5×10^{21} cm^{-2} (see Sousbie 2011), same values used for the Rosette map. The parts used for the profiles in Fig. 8 are indicated with the green dashed lines. The position of the main ionizing sources (O4 and 05 stars) are indicated with the white crosses (Oliveira 2008).

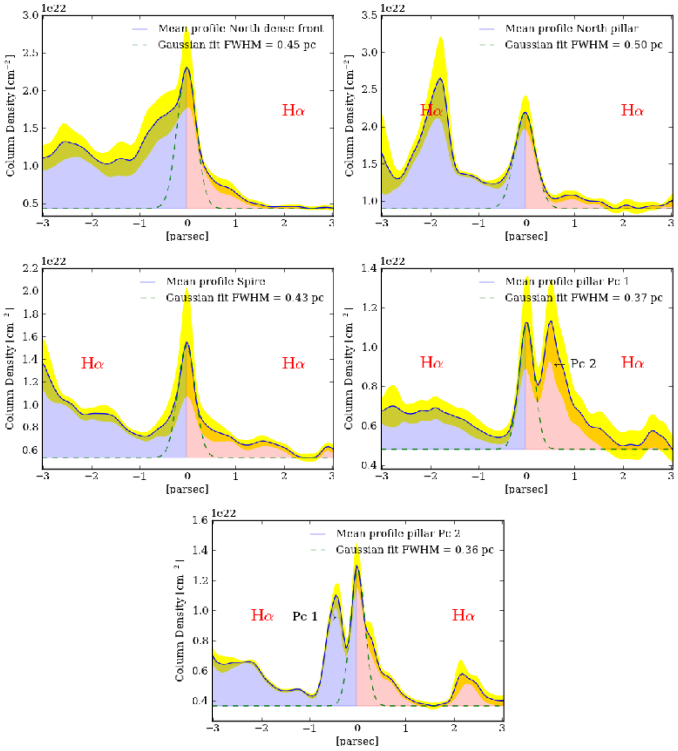

Fig. 8. Profiles of the dense front at the north of the main ionizing sources and profiles of the pillars traced by DisPerSe in M16. The extension of the profiles is fixed at 3 parsecs. The yellow shaded area represents the standard deviation of the profiles. The red sign Hα indicates on which side ionized gas is present (see also Fig. 9 and the Hα emission). The green-dashed curve is the Gaussian fit used to determine the FWHM width.

dense front	FWHM (pc)	σ_{FWHM} (pc)	Asymmetry	σ_{asym}
North front	0.44	0.12	3.3	1.4
North pillar	0.54	0.08	3.4	1.1
Spire	0.45	0.13	2.4	0.8
Pc 1	0.38*	0.09	0.4	0.4
Pc 2	0.35*	0.08	1.8	0.4

Table 2. Deconvolved FWHM width and asymmetric parameter for the averaged profiles of the 5 dense fronts of M16. *The width of the two largest pillars in the three Pillars of Creation is affected by a lack of angular resolution.

cated at the edge or deep into the molecular gas and did not find evidence of any extra source of heating.

Even if the results of Flagey et al. (2011) are confirmed in the future, we do not expect that it will affect our conclusions too much: we concentrate on the kinematic of the cold molecular gas that should be relatively similar regardless of the dominant source of energy (ionization thermal pressure, wind ram pressure, supernova thermal pressure, etc.). The 70 μm data are not used to derive the H_2 column density since it traces small grains in the PDRs instead of the cold dust (Hill et al. 2012). Figure 1 shows as an overview the SPIRE 250 μm map of the M16 cloud, reduced with the pipeline in HIPE10 (see Sect. 2). In Sect. 3.1 we investigate the column density structure of the edge of the molecular cloud, using column density maps at a resolution of 25″ by ignoring the 500 μm emission. This choice is motivated by the width of the pillars in the 70 μm, which is is smaller than their width in the *Herschel* maps at an angular resolution of 37″. In Sect. 3.2 we concentrate on the velocity structure of the head and the base of the three pillars of creation.

3.1. Column density structure

In Hill et al. (2012), the width of the pillars of creation is not resolved in the *Herschel* column density maps that have a resolution of 37″ with the 500 μm data. Indeed, their width traced by the PDR in the 70 μm map is of the order of 25″. By removing the longest wavelength in the column density map, the resolution can be improved to 25″ (limited by the 350 μm data). Figure 7 shows the 25″ *Herschel* column density map of the dense cold regions at the edge of the H II region around NGC 6611. At this resolution, the two largest pillars of the pillars of creation (Pc1 and Pc2), the Spire, and the pillar in the north of the cavity are detected with the DisPerSe algorithm. They appear as disconnected filaments pointing towards the ionizing sources and connected at the base to the rest of the molecular cloud by a triple point in the skeleton. The DisPerSe algorithm connects the largest pillar, Pc1, to the rest of the molecular cloud, although the connection is not obvious in molecular line observations (see White et al. 1999). However, the velocity also suggests that the pillar is still or was connected to the rest of the cloud (see Sect. 3.2). The third pillar (Pc3) of the three pillars of creation is not detected, probably because of the resolution or the threshold in the DisPerSe algorithm. A nascent pillar is also detected in the south of the pillars of creation.

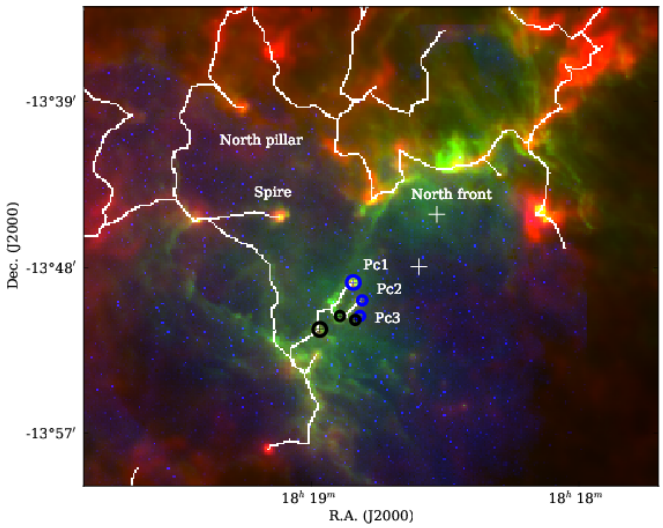

Fig. 9. Three-color image of the interface between the Eagle Nebula and the H II region around NGC 6611 (red: *Herschel* column density map, green: PACS 70 μm, blue: Hα). The white crosses indicate the O stars. Each spectrum in Fig. 10 is integrated inside the corresponding colored circle.

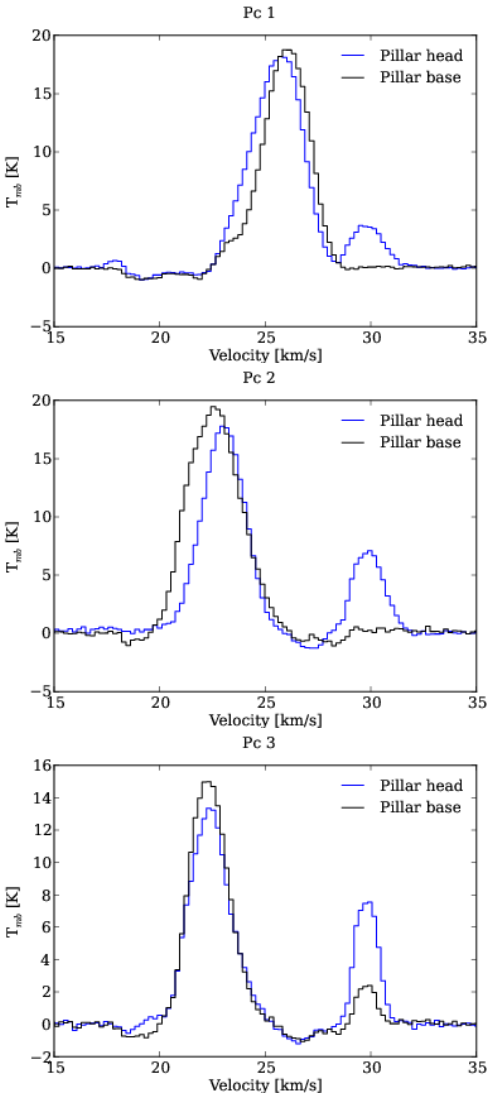

Fig. 10. ^{12}CO 3-2 integrated spectra on the three Pillars of Creation. The spectra are spatially integrated in the colored circles showed in Fig. 9.

Figure 8 presents the averaged column density profiles of the pillars and the profile of the northern front. In the northern region, the compression is clearly visible thanks to the asymmetry of the profile (more than a factor of three between the two sides of the crest, see Table 2). The profiles of the pillars are also asymmetric; however, there is no preferred side, because it depends on the confusion with other structures in the profiles (e.g. Pc1 and Pc2 have reversed asymmetries because they both contribute to the profile of each other). The deconvolved FWHM is also indicated in Table 2. The widths of the two largest pillars of creation are 44″ and 40″, which is almost twice their size as measured in the *Herschel* 70-μm map (resolution of ~6″). The width of the pillars is not properly resolved even if the measured size is twice the size of the beam at 350 μm (25″ resolution).

3.2. Velocity structure

There are only a few high angular resolution spectral-line observations of the whole M16 nebula. The majority of the studies concentrate on the three pillars of creation and SFO30 (the north of the cavity, see Oliveira 2008). Using data from the James Clerk Maxwell Telescope (JCMT[4]) public archives, we examine the velocity structure of the pillars of creation with ^{12}CO (3-2). Figure 9 is a three-colour (Red: *Herschel* column density - Green: 70 μm *Herschel* - Blue: Hα) image around the ionized bubble, where we have indicated the different areas that we selected based on the availability of ^{12}CO (3-2) spectral-line data taken at JCMT. In this work we have analyzed each pillar individually and looked at the differences in the velocity profiles between the head and the base of each of them (see Fig. 10). The blue spectra are integrated around the head of the pillars, and the black ones are integrated around the base.

Pc1 has a bulk velocity around +26 km s^{-1}. As previously mentioned, most observations of the pillars of creation display a gap between the three heads and the rest of the cavity. (The gap is just to the north of the black circle at the base of Pc1 in Fig. 9.) The DisPerSe algorithm, however, connects the pillars to the edge of the cavity based on the contrast level that was used. The connection along Pc1 is also supported here by the velocity spectra that look alike between the two sides of the "gap", while Pc2 and Pc3 have a different bulk velocity around +22.5 km s^{-1}. The difference oinbulk velocity between Pc1 and Pc2/3 has already been seen by White et al. (1999) and may be interpreted as a difference in the orientation and location of the pillars. Indeed, in the *Hubble* image of Hester et al. (1996), Pc1 appears illuminated, while the Pc2 and Pc3 appear dark. This suggests that Pc1 is located behind the ionizing source at the back of the cavity, while Pc2 and Pc3 are between the ionizing source and the observer. The three spectra that are integrated around the heads of the pillars also show a velocity component at 30 km s^{-1}, which probably corresponds to a line-of-sight cloud as claimed by White et al. (1999).

[4] JCMT is operated by the Joint Astronomy Centre on behalf of the Science and Technology Facilities Council of the United Kingdom, the Netherlands Organization for Scientific Research, and the National Research Council of Canada.

The two longest pillars Pc1 and Pc2 have small velocity gradients between the head and the base (see Fig. 10). For Pc1, the head of the pillar is red-shifted at + 0.4 km s^{-1} relative to the base, and for Pc2, the base is red-shifted at + 0.4 km s^{-1} relative to the head. These gradients are projections on the line of sight and could be the result of a change in orientation of the velocity between the head and the base. However, such a gradient perpendicular to the axis of the pillar would mean that the head covered a distance of 0.2 pc in 500 ky away from the rest of the pillar, leading to its destruction. Considering the age of the central cluster, it is much more probable that the velocity field has a constant orientation along the pillar, and the gradients can be interpreted as an increase or decrease in the velocity along the pillar (see also Pound 1998). Considering the Hα illumination, the head of Pc1 is between its base and the observer, therefore the gradient can be interpreted as an extension and a growth of the pillar. Since for Pc2, both the orientation and the gradient are reversed, the pillar also appears to be growing in length. No gradient is observed for Pc3, however the pillar is small and the resolution may not be sufficient to measure a possible gradient between the head and the base of the pillar.

4. Discussion and comparison with numerical simulations

4.1. Large-scale compression from H II regions

The dense fronts around the ionized gas in the Rosette and Eagle nebula are systematically asymmetric with low-density gas where Hα emission is present. This is an indication that these regions are compressed by the ionized gas. This result is similar to those of Peretto et al. (2012) for the Pipe nebula, Schneider et al. (2013) for Orion B, and Nguyên-Luong et al. (2013) for W43-Main. They all found that the gas is compressed by the influence of near-by OB associations. In our two regions, the low density corresponds to the ionized gas from which the material has been swept out, the dense front accumulates the evacuated gas in a dense shell, and the molecular cloud is unperturbed behind the front.

Such compression is also seen in numerical simulations (see Fig. 11). The mean column density profile of the ionization of a turbulent medium with Mach numbers of 1 and 4 (RMS velocity of 0.6 and 2.4 km/s) and a mean density of 500 cm^{-3} is shown in Fig. 12. The simulations include neither gravity nor magnetic fields, the resolution is 0.01 pc, and the heating and cooling function of the cold molecular gas is taken from Wolfire et al. (1995). The heating by the diffuse radiation field in the PDR is neglected, and the heating by the ionization and the cooling by recombination are taken in account when the gas is ionized. The width of the profiles and the compression at the peak position are set by the ratio of the ionized pressure to the turbulent ram pressure (see Tremblin et al. 2012b). In the Mach-1 simulation, the ionized-gas pressure is greater than the turbulent ram pressure, and the compression is efficient, whereas in the Mach-4 simulation, they are within an order of magnitude, and there is almost no compression. Therefore, even if these simulations are not performed in the exact same conditions as the Rosette and Eagle nebulae, it is likely that the ionized-gas pressure is dominant at the edge of these H II regions and leads to the observed compression. Assuming a Larson relation $v_{\rm RMS} = 1.1{\rm km/s}(L_{\rm box}/{\rm pc})^{0.4}$, the RMS velocity on the scale of the box should be around 2 km/s. However, the measured profiles seem to indicate that the level of turbulence is closer to an RMS velocity of $\approx$ 0.6 km/s, this could indicate that the Larson relation is not suitable inside

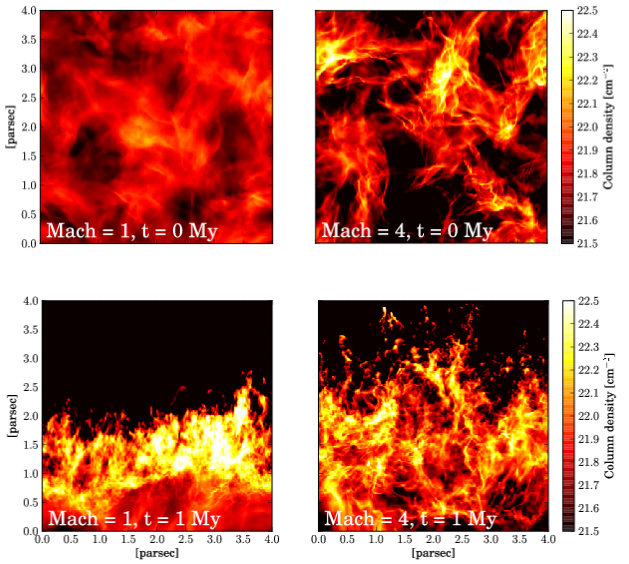

Fig. 11. Column density snapshots of the ionization of a turbulent medium at Mach 1 and Mach 4 (see Tremblin et al. 2012b). The boxes are cubes of 4-pc side at a resolution of 0.01 pc per cell. The initial conditions are a mean density of 500 cm^{-3} and a ionizing flux of 10^9 Lyc photons s^{-1} cm^{-2} coming from the top of the boxes. Top: before the ionization is introduced. Bottom: after 1 My.

a single molecular cloud, as already proposed by Lombardi et al. (2010) for the Larson third law. These compressed profiles are close to what could be expected from the collect process in the collect and collapse scenario proposed by Elmegreen & Lada (1977) and could lead to a sequential star formation. The observed ratio of the column density of the dense fronts to the column density of the unperturbed gas is in the range 4-5 in both regions (background subtracted). If we assume the same density ratios and also dthat the gas is isothermal, the shell velocity given by the Rankine-Hugoniot shock-jump condition would be at $\approx$ 1 km/s ($v^2_{\rm shell}/c^2_0 = n_{\rm shell}/n_0$, with c_0 the sound speed in the cold gas). This is too low for the Rosette nebula whose shell velocity was estimated by Kuchar & Bania (1993) at 4.5 km s^{-1}. However, we have seen in Tremblin et al. (2012b) that the density compression is in the range 10-100 in the Mach-1 simulation, whereas the column-density compression is affected by the projection effect and is only about 3-4 (see Fig. 12). Therefore it is likely that the column-density compression in the Rosette and M16 molecular clouds is also affected by the projection effect and cannot be used to infer the local density compression.

Another indication of the collect process is the difference in the average thickness between the dense fronts 1, 2, and 4 ($\approx$ 0.75 pc) and the dense front 3 and the pillar in the Rosette nebula ($\approx$ 0.55 pc). The standard deviation of the thickness along the fronts is quite large for the dense front 3, therefore this result needs further investigation.The fronts 1, 2, and 4 are perpendicular to the propagation of the shell and therefore can collect a large amount of material on the way along their length. For the pillar and the front 3, they are parallel to the direction of expansion and can only collect material along their width, which is relatively small. Therefore the mass of these structures cannot grow as much as the rest of the shell. This could explain why their width is smaller than the width of the other dense fronts that should be able to grow as a function of time.

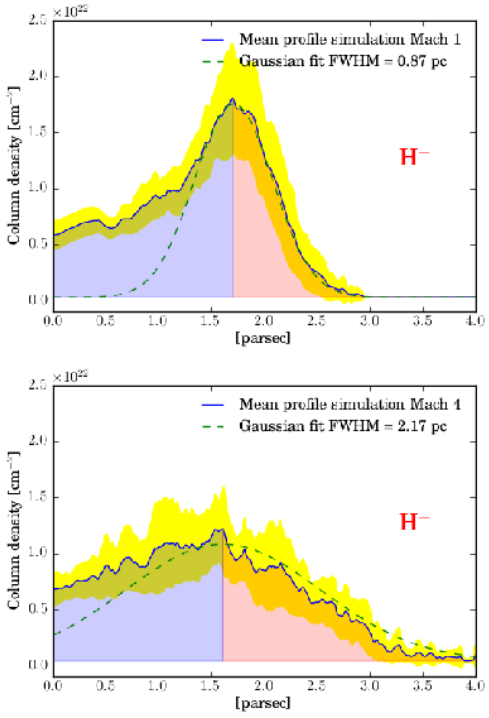

Fig. 12. Column density profiles of the two simulations shown in fig. 11 after 1 My. The red sign H^+ indicates the position of the ionized gas in the simulation. The flux is coming from the right side of the profiles.

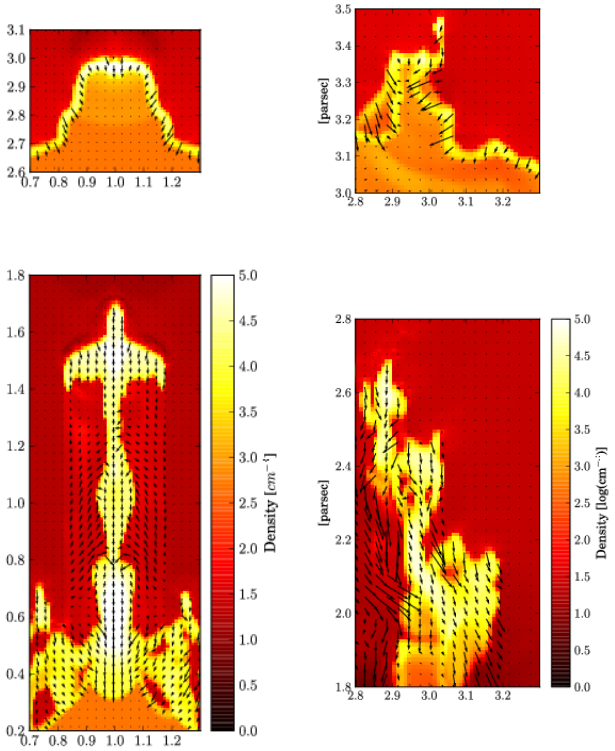

Fig. 13. Density cut of the formation of a pillar in an idealized simulation of a clump embedded in a homogeneous medium (left : Tremblin et al. 2012a) and in a turbulent medium at Mach 1 (right: Tremblin et al. 2012b). The black arrows represent the velocity field of the neutral gas. The compressed layer can be identified with the velocity field and the high density (around 10^4 cm^{-3} in yellow). Top: the snapshots are taken when the pillar is forming, just before the compressed layer has collapsed in on itself. The high curvature of the compressed layer can be clearly identified in both cases. Bottom: after the shell has collapsed, the pillars are formed.

4.2. From nascent to old pillars

With the DisPerSe algorithm, it is possible to detect pillars as fronts with one side disconnected and pointing towards the ionizing source and the other side connected at the base to the rest of the cavity. Long pillars (pillars of creation, the Spire, etc.) are detected well by this process. This method is also useful for detecting small pillars at the edge of the cavity, whic are possibly at the earliest phase of their formation process. Such nascent pillars can be detected in the Rosette and the Eagle nebula. In Tremblin et al. (2012a), the key ingredient for the formation of pillars is the high curvature of the shell that collapses in on itself. A clear observational diagnostic that has been derived is a red-shifted and a blue-shifted component that should appear in the velocity spectrum of the nascent pillar as a signature of the collapse of the shell on itself (see Figs. 14 and 13, before the collapse). The same process was also identified in turbulence simulations (see Tremblin et al. 2012b). This signature has recently been confirmed by simulations with synthetic observations in ^{12}CO and ^{13}CO performed by Haworth et al. (2013). All of these simulations converge to highlight the collapse of the shell on itself as the key process in forming a pillar. Remarkably, the nascent pillar in the Rosette nebula detected by the DisPerSe algorithm presents such a spectrum in ^{13}CO (1-0). The same structure can also be seen in the ^{12}CO (1-0) data, as expected from the synthetic observations in Haworth et al. (2013). Two central components at +13 and +14 km s^{-1} are associated with the velocity components of the front east and west of the nascent pillar. In addition to these central components, a red-shifted component is present at +19 km s^{-1} and a blue-shifted one at +11 km s^{-1}. The model in Tremblin et al. (2012a) predicts that the velocity shift between the two peaks is around twice the shell velocity if the line of sight is aligned with the velocity of the collapsing fragments. If not, the shell velocity is greater than half the velocity shift because of the line-of-sight projection. The channel maps in Fig 6 show that the 9-12 km/s and 17-21 km/s components are not spatially aligned, so we expect a projection effect on the velocity. Accordingly, we expect a shell velocity higher than 4 km s^{-1}. If we assume it to be correct that the shell velocity is measured by Kuchar & Bania (1993) at 4.5 km/s, we can estimate that the velocities of the collapsing fragments have an angle of $\approx 25°$ with the line of sight.

In Tremblin et al. (2012a) and Tremblin et al. (2012b), evolved pillars have a simpler velocity distribution, i.e., a single peak that is centred on the velocity of the shell (see Figs. 13 and 14). From the base, the velocity decreases along the pillar down to the head. The gradient leads to a growth of the pillar as a function of time over more than 1 My. More recent simulations (Tremblin et al. in prep.) have shown that, at later times, the head is accelerated thanks to the rocket effect. Since the velocity at the base of the pillar decreases as a function of time, the head can be accelerated to velocities greater than the velocity of the base. At this point, the pillar shrinks and can even be destroyed when the head reaches the rest of the dense front. The spectra of the pillars in the Rosette and Eagle nebula present a single-peak spectrum and a gradient between the head and the base. Using

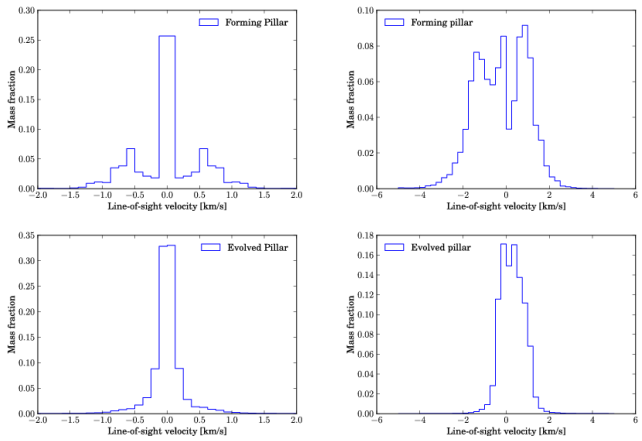

Fig. 14. Distribution of the gas mass as a function of the line-of-sight velocity for the snapshots in Fig. 13. Top: the spectra are taken when the pillar is forming and the shell curved, just before the shell has collapsed in on itself. The blue- and red-shifted components can be clearly identified in both cases and are associated with the curved shell. Bottom: after the collapse, when the pillar is in its growing state, the spectra display a single peak.

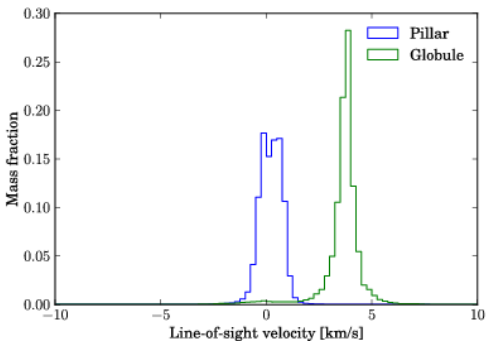

Fig. 15. Distribution of the gas mass as a function of the line-of-sight velocity for a pillar in the Mach-1 simulation and for a globule in the Mach-4 simulation (see Tremblin et al. 2012b, for the details of the numerical setup.). Snapshots of the Mach 1 and Mach 4 simulations are in Fig.11).

the Hα emission to examine the orientation of the pillar, we are able to conclude that the pillars are growing. Therefore they are evolved pillars still in a phase of growth, and their heads are not accelerated at velocities higher than the velocity of the shell.

4.3. Turbulent globules

Tremblin et al. (2012b) determined a link between the formation of globules in H II regions and the initial turbulence of the molecular cloud. The process is relatively simple: When the ram pressure of the turbulence is greater than the pressure of the ionized gas, some parts of cold gas have enough kinetic energy to penetrate the H II region. Since their velocity is dominated by the turbulence, they have a random component that is perpendicular to the direction of expansion of the bubble, causing them to detach from the molecular cloud and form a cometary globule. Their transverse random velocity can be used as observational diagnostics: pillars, dense fronts, and condensations have a motion in the direction of pressure-driven expansion of the bubble. In contrast, globules will have a random motion that will lead to large shifts in their bulk velocity compared to the velocity of nearby dense fronts (see Fig. 15). Such a shift has already been observed in Schneider et al. (2012b) between a globule and the nearby pillars at the edge of the ionized gas around Cygnus OB2.

In the Rosette nebula, we observed two globules near the dense front 2. The Hα emission shows that this proximity is not a projection effect. The velocity spectra of these globules are shifted at + 3 km s^{-1} and + 6 km s^{-1} relative to the dense front, and since the structures are close, these shifts can be interpreted as the relic of the initial turbulence.

5. Conclusions

Combining continuum and spectral line data, we are able to constrain the dynamics of the gas at the edge of H II regions in the Rosette and Eagle nebulae.

- The column-density dense fronts at the interface with the ionized gas present a compressed asymmetric profile with a width that is consistent with numerical simulations whose key ingredients are turbulence and ionization.
- A crest-detection algorithm is an efficient tool for outlining pillars in the column density maps. The velocity structures of these pillars are consistent with numerical simulations. Especially the detection of a nascent pillar in the Rosette nebula was possible, and its velocity profile presents blue-shifted and red-shifted components in ^{12}CO and ^{13}CO. This type of profile was predicted in numerical simulations as the signature of the collapse of the shell in on itself, the first step in forming a pillar. The comparison of the simulations and the observations in this paper confirms that this as a new scenario for the formation of pillars.
- Existing numerical simulations show that globules tend to be formed when the turbulent ram pressure is greater than the ionized-gas pressure. When the turbulence dominates, some parts of the cold gas have enough kinetic energy to penetrate the ionized region and form cometary globules. Because of the link with turbulence, these globules have a random bulk velocity set by the initial turbulence, which can be perpendicular to the direction of the shell expansion. Such dispersed bulk velocities are observed for the globules in the Rosette nebula, thus confirming their turbulent origin.

The observations presented in this paper converged with previous numerical works to give a clear picture of the formation of pillars and globules around H II regions, which are curved and collapsing parts of the shells induced by pre-existing structures for pillars and turbulent gas motion for globules. Gravity-based scenarios, such as the Rayleigh Taylor instability first proposed by Spitzer (1954), or more recently, the remains of an accretion flow (Dale et al. 2012), are ruled out by the velocity field structure in the case of the pillars of creation. Indeed, Frieman (1954) showed that the effect of gravity would lead to a free-fall profile for the velocity field; i.e., the velocity is proportional to the square root of the distance along the pillar, and Pound (1998) invalidated this possibility for the pillars of creation. All previous models do not predict a collapsing shell that is observed in the case of the nascent pillar in the Rosette nebula. The structures both in M16 and Rosette are consistent with the interaction between ionization and turbulence, and other scenarios might still happen in other regions, therefore more observations are needed in order to confirm whether these two new models are ubiquitous in galactic molecular clouds.

A direct consequence of this pillar formation scenario is that a pre-existing dense clump will curve the shell around it, triggering the collapse and the formation of a pillar, while a low-density perturbation will not curve the shell enough to trigger the collapse. Instead, a dense clump is subsequently formed in the shell by the accumulation of matter triggered by the perturbation. This effect has been simulated in Tremblin et al. (2012a) and also in Minier et al. (2013) in the special case of RCW36. Therefore, star formation happening at the tip of pillars is likely to have happened even without ionization, while star formation in dense clumps in the shell is likely to be triggered by the feedback (see also Dale et al. 2013). With the recent statistics of YSOs located at the edge of ionized bubbles (e.g. Thompson et al. 2012), it becomes clear that star formation triggered by the feedback of massive stars is indeed frequent and an important ingredient for understanding galactic star formation.

Acknowledgements. SPIRE has been developed by a consortium of institutes led by Cardiff Univ. (UK) and including: Univ. Lethbridge (Canada); NAOC (China); CEA, LAM (France); IFSI, Univ. Padua (Italy); IAC (Spain); Stockholm Observatory (Sweden); Imperial College London, RAL, UCL-MSSL, UKATC, Univ. Sussex (UK); and Caltech, JPL, NHSC, Univ. Colorado (USA). This development has been supported by national funding agencies: CSA (Canada); NAOC (China); CEA, CNES, CNRS (France); ASI (Italy); MCINN (Spain); SNSB (Sweden); STFC, UKSA (UK); and NASA (USA). PACS has been developed by a consortium of institutes led by MPE (Germany) and including UVIE (Austria); KU Leuven, CSL, IMEC (Belgium); CEA, LAM (France); MPIA (Germany); INAF-IFSI/OAA/OAP/OAT, LENS, SISSA (Italy); IAC (Spain). This development has been supported by the funding agencies BMVIT (Austria), ESA-PRODEX (Belgium), CEA/CNES (France), DLR (Germany), ASI/INAF (Italy), and CICYT/MCYT (Spain). Part of this work was supported by the ANR-11-BS56-010 project "STARFICH".

References

Allen, L. E., Burton, M. G., Ryder, S. D., Ashley, M. C. B., & Storey, J. W. V. 1999, MNRAS, 304, 98
Arthur, S. J., Henney, W. J., Mellema, G., De Colle, F., & Vázquez-Semadeni, E. 2011, MNRAS, 414, 1747
Arzoumanian, D., André, P., Didelon, P., et al. 2011, A&A, 529, L6
Bertoldi, F. 1989, ApJ, 346, 735
Bisbas, T. G., Wünsch, R., Whitworth, A. P., Hubber, D. A., & Walch, S. 2011, ApJ, 736, 142
Blaauw, A. 1991, The Physics of Star Formation and Early Stellar Evolution, 125
Bonatto, C., Santos, J. F. C. J., & Bica, E. 2006, A&A, 445, 567
Carlhoff, P., Luong, Q. N., Schilke, P., et al. 2013, arXiv, 6112
Cox, P., Deharveng, L., & Leene, A. 1990, A&A, 230, 181
Dale, J. E., Ercolano, B., & Bonnell, I. A. 2012, Monthly Notices of the Royal Astronomical Society, 427, 2852
Dale, J. E., Ercolano, B., & Bonnell, I. A. 2013, MNRAS, 431, 1062
Deharveng, L., Schuller, F., Anderson, L. D., et al. 2010, A&A, 523, 6
Deharveng, L., Zavagno, A., Schuller, F., et al. 2009, A&A, 496, 177
Di Francesco, J., Sadavoy, S., Motte, F., et al. 2010, A&A, 518, L91
Elmegreen, B. G. & Lada, C. J. 1977, ApJ, 214, 725
Flagey, N., Boulanger, F., Noriega-Crespo, A., et al. 2011, A&A, 531, 51
Frieman, E. A. 1954, ApJ, 120, 18
Gritschneder, M., Burkert, A., Naab, T., & Walch, S. 2010, ApJ, 723, 971
Haworth, T. J. & Harries, T. J. 2011, MNRAS, 2003
Haworth, T. J., Harries, T. J., Acreman, D. M., & Rundle, D. A. 2013, MNRAS, 431, 3470
Hennemann, M., Motte, F., Bontemps, S., et al. 2010, A&A, 518, L84
Hennemann, M., Motte, F., Schneider, N., et al. 2012, A&A, 543, L3
Hester, J. J., Scowen, P. A., Sankrit, R., et al. 1996, Astronomical Journal v.111, 111, 2349
Heyer, M. H., Williams, J. P., & Brunt, C. M. 2006, ApJ, 643, 956
Hildebrand, R. H. 1983, Quarterly Journal of the Royal Astronomical Society, 24, 267
Hill, T., Motte, F., Didelon, P., et al. 2012, A&A, 542, 114
Kuchar, T. A. & Bania, T. M. 1993, ApJ, 414, 664
Linsky, J. L., Gagné, M., Mytyk, A., McCaughrean, M., & Andersen, M. 2007, ApJ, 654, 347
Lombardi, M., Alves, J., & Lada, C. J. 2010, A&A, 519, L7
Mackey, J. & Lim, A. J. 2010, MNRAS, 403, 714
Mellema, G., Arthur, S. J., Henney, W. J., Iliev, I. T., & Shapiro, P. R. 2006, ApJ, 647, 397
Miao, J., Sugitani, K., White, G. J., & Nelson, R. P. 2010, ApJ, 717, 658
Miao, J., White, G. J., Nelson, R., Thompson, M., & Morgan, L. 2006, MNRAS, 369, 143
Miao, J., White, G. J., Thompson, M. A., & Nelson, R. P. 2009, ApJ, 692, 382
Minier, V., Tremblin, P., Hill, T., et al. 2013, A&A, 550, 50
Motte, F., Zavagno, A., Bontemps, S., et al. 2010, A&A, 518, L77
Nguyên-Luong, Q., Motte, F., Carlhoff, P., et al. 2013, ApJ, 775, 88
Oliveira, J. M. 2008, Handbook of Star Forming Regions, I, 599
Peretto, N., André, P., Könyves, V., et al. 2012, A&A, 541, 63
Poulton, C. J., Robitaille, T. P., Greaves, J. S., et al. 2008, MNRAS, 384, 1249
Pound, M. W. 1998, Astrophysical Journal Letters v.493, 493, L113
Roussel, H. 2012, Astrophysics Source Code Library, 09012
Schneider, N., André, P., Könyves, V., et al. 2013, ApJ, 766, L17
Schneider, N., Csengeri, T., Hennemann, M., et al. 2012a, A&A, 540, L11
Schneider, N., Güsten, R., Tremblin, P., et al. 2012b, A&A, 542, L18
Schneider, N., Motte, F., Bontemps, S., et al. 2010, A&A, 518, L83
Schneider, N., Stutzki, J., Winnewisser, G., & Block, D. 1998a, A&A, 335, 1049
Schneider, N., Stutzki, J., Winnewisser, G., Poglitsch, A., & Madden, S. 1998b, A&A, 338, 262
Schuller, F., Leurini, S., Hieret, C., et al. 2006, A&A, 454, L87
Sousbie, T. 2011, MNRAS, 414, 350
Spitzer, L. J. 1954, Astrophysical Journal, 120, 1
Thompson, M. A., Urquhart, J. S., Moore, T. J. T., & Morgan, L. K. 2012, MNRAS, 421, 408
Thompson, M. A., White, G., Morgan, L. K., et al. 2004, A&A, 414, 1017
Tremblin, P., Audit, E., Minier, V., & Schneider, N. 2012a, A&A, 538, 31
Tremblin, P., Audit, E., Minier, V., Schmidt, W., & Schneider, N. 2012b, A&A, 546, 33
Urquhart, J. S., White, G. J., Pilbratt, G. L., & Fridlund, C. V. M. 2003, A&A, 409, 193
Walch, S., Whitworth, A. P., Bisbas, T. G., Wünsch, R., & Hubber, D. A. 2013, arXiv
White, G. 1993, A&A, 274, L33
White, G. & Gee, G. 1986, A&A, 156, 301
White, G., Nelson, R. P., Holland, W. S., et al. 1999, A&A, 342, 233
Williams, J. P., de Geus, E. J., & Blitz, L. 1994, ApJ, 428, 693
Wolfire, M. G., Hollenbach, D., McKee, C. F., Tielens, A. G. G. M., & Bakes, E. L. O. 1995, ApJ, 443, 152

[1] Laboratoire AIM Paris-Saclay (CEA/Irfu - Uni. Paris Diderot - CNRS/INSU), Centre d'études de Saclay, 91191 Gif-Sur-Yvette, France
[2] Astrophysics Group, University of Exeter, EX4 4QL Exeter, UK
[3] Univ. Bordeaux, LAB, UMR 5804, F-33270, Floirac, France
[4] CNRS, LAB, UMR 5804, F-33270, Floirac, France
[5] Maison de la Simulation, CEA-CNRS-INRIA-UPS-UVSQ, USR 3441, Centre détude de Saclay, 91191 Gif-Sur-Yvette, France
[6] School of Physics and Astronomy, Cardiff University, Queens Buildings, The Parade, Cardiff CF24 3AA, UK
[7] IAS, CNRS (UMR 8617), Université Paris-Sud, Bâtiment 121, 91400 Orsay, France
[8] Aix Marseille Université, CNRS, LAM (Laboratoire d'Astrophysique de Marseille) UMR 7326, 13388, Marseille, France
[9] Department of Physics, West Virginia University, Morgantown, WV 26506, USA
[10] Université de Toulouse, UPS, CESR, 9 avenue du Colonel Roche, CNRS, UMR 5187, 31028 Toulouse Cedex 4, France
[11] Max-Planck-Institut für Radioastronomie, Auf dem Hügel 69, 53121 Bonn, Germany
[12] National Research Council of Canada, Herzberg Institute of Astrophysics, 5071 West Saanich Road, Victoria, BC V9E 2E7, Canada
[13] INAF IAPS, via Fosso del Cavaliere 100, 00133 Roma, Italy
[14] European Space Astronomy Centre, Urb. Villafranca del Castillo, PO Box 50727, E-28080 Madrid, Spain
[15] Canadian Institute for Theoretical Astrophysics, University of Toronto, 60 St. George Street, Toronto, ON M5S 3H8, Canada
[16] Université de Toulouse; UPS-OMP; IRAP; Toulouse, France
[17] CNRS; IRAP; 9 Av. colonel Roche, BP 44346, F-31028 Toulouse cedex 4, France
[18] Institut d'Astrophysique de Paris, Université Pierre et Marie Curie (UPMC), CNRS (UMR 7095), 75014 Paris, France
[19] APS-INAF, Fosso del Cavaliere 100, I-00133 Roma, Italy
[20] The Rutherford Appleton Laboratory, Chilton, Didcot, OX11 0NL, UK
[21] Department of Physics and Astronomy, The Open University, Milton Keynes, UK
[22] Institute for Astronomy, University of Hawaii, 96822 Honolulu, Hawaii